

## THE STRUCTURE AND APPEARANCE OF PROTOSTELLAR ACCRETION DISKS: LIMITS ON DISK FLARING

K. R. BELL<sup>1</sup> AND P. M. CASSEN

Space Sciences Division, NASA/Ames Research Center, NASA/Ames Research Center, MS 245-3, Moffett Field, CA 94035;  
 bell@cosmic.arc.nasa.gov, cassen@cosmic.arc.nasa.gov

AND

H. H. KLAHR AND TH. HENNING

Max Planck Society, Research Unit “Dust in Star-Forming Regions”, Schillergäßchen 3 D-07745 Jena, Germany;  
 klahr@astro.uni-jena.de, henning@astro.uni-jena.de

Received 1997 January 15; accepted 1997 April 3

### ABSTRACT

Vertical structure models are used to investigate the structure of protostellar,  $\alpha$ -law, accretion disks. Conditions investigated cover a range of mass fluxes ( $10^{-9}$  to  $10^{-5} M_{\odot} \text{ yr}^{-1}$ ), viscous efficiencies ( $\alpha = 10^{-2}$  and  $10^{-4}$ ), and stellar masses ( $0.5$ – $3 M_{\odot}$ ). Analytic formulae for midplane temperatures, optical depths, and volume and surface densities are derived and are shown to agree well with numerical results. The temperature dependence of the opacity is shown to be the crucial factor in determining radial trends. We also consider the effect on disk structure of illumination from a uniform field of radiation such as might be expected of a system immersed in a molecular cloud core or other star-forming environment:  $T_{\text{amb}} = 10, 20$ , and  $100$  K. Model results are compared to *Hubble Space Telescope* observations of HH30 and the Orion proplyds.

Disk shape is derived in both the Rosseland mean approximation and as viewed at particular wavelengths ( $\lambda\lambda = 0.66, 2.2, 60, 100, 350$ , and  $1000 \mu\text{m}$ ). In regions where the opacity is an increasing function of temperature (as in the molecular regions where  $\kappa \propto T^2$ ), the disk does not flare, but decreases in relative thickness with radius under both Rosseland mean and single wavelength approximations. The radius at which the disk becomes shadowed from central object illumination depends on radial mass flow and varies from a few tenths to about  $5$  au over the range of mass fluxes tested. This suggests that most planet formation occurred in environments unheated by stellar radiation. Viewing the system at any single wavelength increases the apparent flaring of the disk but leaves the shadow radius essentially unchanged. External heating further enhances flaring at large radii, but, except under extreme illumination ( $100$  K), the inner disk will shield the planet-forming regions of all but the lowest mass flux disks from radiation originating near the origin such as from the star or from an FU Orionis outburst.

*Subject headings:* accretion, accretion disks — radiative transfer — stars: pre-main-sequence

### 1. INTRODUCTION

There is abundant evidence that accretion disks are common around pre-main-sequence stars, and it is likely that the solar nebula was such a disk at the time the planets and other bodies of the solar system were forming. The details of the temperature and density structure during the accretion phase are therefore of great interest in developing theories of the formation and evolution of planetary systems like our own. Of particular interest is the balance between locally generated and externally provided energy. Locally generated energy is released as matter is radially transported inward. Inward migration of matter is accompanied by local dissipation and the outward transport of angular momentum. External sources of energy include the isotropic background radiation field from the surrounding molecular cloud and directed illumination from the central star, boundary layer, and inner disk. This last contribution may be particularly important during the short-lived ( $\approx 100$  yr) but luminous ( $L_{\text{FU}} \approx 100L_{\text{TT}}$ ) FU Orionis outbursts in which the inner  $\frac{1}{4}$  au of the protostellar disk brightens to become the principal source of emitted radiation (Hartmann & Kenyon 1996, and references therein). All sources of radiation originating at small radius ( $r \lesssim \frac{1}{3}$  au)

whether star, boundary layer, or inner disk will be referred to collectively as the “central object.”

In this paper we explore radial temperature and density profiles of disks with various accretion rates, viscous efficiencies, stellar masses, and ambient radiation fields and provide analytic formulae based on an analytic Rosseland mean opacity, which provide excellent matches to numerically derived results. We further calculate the disk shape both in the Rosseland mean approximation and using detailed frequency-dependent opacities which, when combined with disk atmosphere calculations ( $\tau_{\text{R}} \ll \frac{2}{3}$ ), result in observable disk profiles at several selected wavelengths:  $\lambda\lambda = 0.66, 2.3, 60, 100, 350$ , and  $1000 \mu\text{m}$ . The effect of uniform background irradiation temperatures of  $10, 20$ , and  $100$  K is investigated. Silhouettes of edge-on disk models are compared to recent *Hubble Space Telescope* observations of HH30 and the Orion Proplyds. Although we do not explicitly include the effects of directed sources of illumination, we discuss the implications of the resulting disk shapes for potential illumination by a source at the center of the system. We conclude that in all but the lowest mass flux disks, most of the disk will be shielded at all wavelengths from central object radiation.

Our method will exploit some of the more general results of accretion disk theory, which was first developed in detail by Lüst (1952), and later by Lynden-Bell & Pringle (1974)

<sup>1</sup> University of California at Santa Cruz.

and others. Dissipative interactions between adjacent annuli, such as those caused by turbulent viscosity, transport angular momentum outward, thereby allowing mass in the inner part of the disk to flow inward. If the mass flow through the disk  $\dot{M}$  is the same at all radii, and the dissipated energy is radiated locally (i.e., vertical transport of energy to the surfaces of the disk predominates over radial transport), an internally produced accretion flux ensues:

$$\sigma T_{\text{acc}}^4 \equiv \frac{3\dot{M}\Omega^2}{8\pi} \left(1 - \sqrt{\frac{R_*}{r}}\right), \quad (1)$$

where  $\Omega^2 = GM_*/r^3$  and  $M_*$  and  $R_*$  are stellar mass and radius, respectively. This flux is independent of the uncertain value of the effective viscosity (Lynden-Bell & Pringle 1974). A parameterization for viscous transport introduced by Shakura & Sunyaev (1973), in which the kinematic viscosity  $\nu$  is assumed proportional to the local sound speed  $c_s$  and scale height  $h$  times an efficiency factor  $\alpha_s$ :

$$\nu = \alpha_s c_s h, \quad (2)$$

allows the development of quantitative models that explore conditions in the unobservable disk midplane (e.g., Lin & Papaloizou 1980; Pringle 1981; Ruden & Lin 1986; Ruden & Pollack 1991).

Disks may be expected to approach the radially constant mass flux condition given sufficient time to rearrange matter and to dissipate radial inhomogeneities. Nevertheless, there must always exist some material in the outermost part of the disk that is the ultimate recipient of the angular momentum given up by the inward flowing material at smaller radii, and consequently flows outward. Thus, the mass flow cannot be independent of radius over the entire disk. The radius,  $R_a$ , at which the radial mass flux changes from inward to outward (the “turn-around” radius) constantly grows with time. Within  $R_a$ , equation (1) provides a good representation of the internally generated accretion flux; beyond  $R_a$ , the radiated energy diminishes with radius much more rapidly than  $r^{-3}$ . For instance, in a similarity solution with no central couple explored by Lynden-Bell & Pringle (1974), dissipation decreases exponentially beyond the turn-around point principally because of the rapidly decreasing surface density there (their eq. [24]); in this formulation,  $R_a^2 = 0.75\nu M_D/\dot{M} \approx 0.75\nu t$ , where  $M_D$  is the total disk mass and  $t$  is the time elapsed. Our constant mass flux models are only expected to apply in regions interior to  $R_a$ , the exact value of which depends on the age of the nebula and on the value of the viscosity. Some values of  $R_a$  for viscosities typical of the calculations in this work are shown in Table 1.

External energy may be provided by the central object. Although it is commonly assumed that disks are exposed at all radii to such radiation by virtue of the disk being either

flat and infinitesimally thin (e.g., Adams, Lada, & Shu 1987) or monotonically flaring (i.e.,  $H \propto r^q$ , where  $q > 1$  for all radii;  $q = 9/8$  or  $5/4$ , Kenyon & Hartmann 1987), neither of these assumptions is entirely self-consistent. In the case of the flat disk, the absolute absence of any atmosphere above the disk midplane must be assumed or light from the star will be extinguished as it travels to large radii nearly parallel to the disk’s surface. In a flaring disk, progressive extinction is less important, but it remains to be shown that disks do indeed increase in scale height to arbitrarily large radius. For protostellar disks (Ruden & Pollack 1991) and for disks around cataclysmic variables (Meyer & Meyer-Hofmeister 1982) numerical models have  $q > 1$  out to a given radius beyond which the disk turns concave downward. Outer annuli are consequently cast into shadow.

Star/disk systems do not, however, exist in isolation. Young disks ( $\lesssim 10^6$  yr; Strom, Edwards, & Skrutskie 1993) are surrounded by and still receive matter from the molecular cloud cores from which they condensed. Disks cannot be any cooler than the ambient medium. Estimates of these temperatures must account for the influence of the formation of the star itself (e.g., Adams & Shu 1985; Chick, Pollack, & Cassen 1996; d’Alessio, Calvet, & Hartmann 1997). Prior to star formation, molecular cloud cores range from 10 to 20 K in the cooler Taurus regions (van Dishoeck et al. 1993) to 100 K or more in the hot Orion type regions. Temperatures observed from  $\text{NH}_3$  emission within a few hundred au around the protostar IRAS 16293–2422 are in the range of 15–20 K (Mundy, Wootten, & Wilking 1990). Disks in the neighborhood of high mass stars such as in the well-studied Orion Nebula may see much higher illumination on the order of 100–200 K. Because other sources of energy diminish with distance from the central object, the ambient medium must eventually determine the thermal state of disks at large distances. Consider the stellar radiation reprocessed in a thin, flat disk: Far from the star, its equivalent temperature is given by

$$T_{rp}^4(r) = \frac{2}{3\pi} T_*^4 \left(\frac{R_*}{r}\right)^3 \quad (3)$$

(Safronov 1960; Ruden & Pollack 1991). For a rather luminous star with  $T_* = 4000$  K and  $R_* = 3 R_\odot$  ( $\approx 8 L_\odot$ ), the radius at which the ambient field becomes more important than the directed radiation from the central object is about 10 au, where  $T_{\text{amb}} = 20$  K and 1 au, where  $T_{\text{amb}} = 100$  K. In most molecular cloud core regions, the ambient temperature is therefore more important than stellar illumination in determining large scale disk structure.

Infalling material also provides an energy source at the surface of the disk, as it is decelerated through an accretion shock and mixes with disk material. The vertical, radial, and a fraction of the azimuthal velocity components of the infalling gas are destroyed, and one-half of the energy released shines on the disk. This flux diminishes with radius as  $r^{-2}$  for the collapse of a uniformly rotating isothermal sphere (Cassen & Moosman 1981). If the accretion rate through the disk keeps up with the rate at which collapsing material arrives, both the internally generated energy and the reprocessed radiation from the central object are generally greater than the shock-released energy (Cassen & Moosman 1981; Chick et al. 1996).

Because there is some ambiguity in nomenclature, it is

TABLE 1  
TURN-AROUND RADIUS (au)

TIME (yr)	VISCOSITY ( $\text{cm}^2 \text{s}^{-1}$ )		
	$10^{15}$	$10^{16}$	$10^{17}$
$10^4$ .....	1.0	3.2	10
$10^5$ .....	3.2	10	32
$10^6$ .....	10	32	100

worth discussing three distinct, commonly used definitions of “disk thickness” before proceeding to a description of the models. First, for all definitions of thickness, when we refer to the “relative” thickness of the disk, we mean its local thickness divided by the radial distance of the annulus from the center of the system,  $H/r$ , as opposed to its absolute thickness,  $H$ .

Throughout this paper we will generally understand the “thickness” of a radial annulus to be the *distance above the midplane of the Rosseland mean photosphere*, or its “photospheric thickness” designated by  $H_R$ . Rosseland mean optical depths are designated  $\tau_R$ . The photosphere is taken to be that point at which, integrating from infinity, traveling perpendicular to the disk midplane, one reaches  $\tau_R = \frac{2}{3}$ . The Rosseland mean opacity indicates the dominant avenue of radiation for optically thick material (e.g., Pollack et al. 1994). In other words, an optically thick medium radiates energy principally at the wavelength corresponding, through the Wien law ( $\lambda T = 0.29$  cm K), to the temperature of the Rosseland mean photosphere. This wavelength varies strongly with radius throughout most of the disk where the surface temperature is not radially constant. Energy incident onto the surface of the disk may have been created at a very different temperature than the material it intercepts and would therefore dominate at a very different wavelength. Consider, for example, an annulus at 5 au with a central star with  $R_* = 3 R_\odot$ ,  $T_* = 4000$  K and an ambient field of  $T_{\text{amb}} = 20$  K. Stellar radiation (though much diminished in magnitude by distance) will peak at  $7250 \text{ \AA}$ , while the ambient field radiation will peak at  $145 \text{ }\mu\text{m}$ . Meanwhile, the disk (assumed for the moment to be thin, flat, and devoid of internal sources of energy) will reprocess a combination of the two sources of energy and radiate at 34 K with a corresponding wavelength of  $85 \text{ }\mu\text{m}$ .

In general, shorter wavelengths see higher opacities, so short-wavelength photons are absorbed higher up in the disk atmosphere than are longer wavelength photons. This effect motivates a second definition of thickness, which is *the thickness as seen at a given wavelength*,  $H_\lambda$ , or the distance perpendicular above the midplane at which an incoming photon of a given wavelength  $\lambda$  will experience an optical depth of  $\tau_\lambda = \frac{2}{3}$ . This thickness will be designated  $H_\lambda$ , where  $\lambda$  is given in microns. This definition will be particularly useful for comparing disk models to observations taken at a particular wavelength. In both of these definitions of disk thickness, the disk is assumed to be viewed exactly face-on, i.e., radiation travels only perpendicular to the disk midplane. When viewed at an angle or when receiving radiation from a glancing source (e.g., the central object), the apparent disk surface must be appropriately modified and further, the radial temperature and density profile of the disk and its atmosphere must be taken into account (e.g., Malbet & Bertout 1991; Men’shchikov & Henning 1997).

A third definition of thickness is *the distance above the midplane at which the pressure or density has dropped by the factor  $e$* , i.e., the disk’s pressure or density scale height. We will refer to this quantity as  $h$ . Although this altitude marks a density significantly lower than the midplane value, there is no *a priori* reason to assume that this corresponds to a physical disk photosphere of any kind. Nevertheless, in § 4 we show that in the regions where the disk is optically thick to its own radiation, i.e., where  $\tau_R \gg \frac{2}{3}$ ,  $H_R \approx (2-3) \times h$ .

From the condition of hydrostatic equilibrium,  $h$  is given by

$$h \approx \frac{c_s}{\Omega} \quad (4)$$

(Pringle 1981). The radial trend of scale height thus depends principally on the steepness of the radial temperature profile:  $h \propto (Tr^3)^{1/2}$ . In the outer, isothermal disk, where radiation is dominated by the ambient field, the pressure scale height increases strongly with radius:  $h \propto r^{3/2}$ .

In this paper, we investigate radial trends of the thickness of axisymmetric,  $\alpha$ -law viscosity, constant mass flux, accretion disks under the assumption that annuli may be independently calculated. Details of our numerical method are described in the § 2. Our results in terms of the midplane temperatures, densities, and optical depths are presented in § 3. Analytic formulae are derived in several subsections, and results of these simple derivations are shown to agree well with numerical results. Radial trends in self-gravity and convection are also discussed. The radial trend of disk thickness in both the Rosseland mean approximation and at particular wavelengths is discussed in § 4. It is shown analytically and numerically that these disks are expected to reach a peak in  $H_R/r$  at a modest radius then become concave down shielding themselves from radiation emanating from the inner parts of the system. Also in this section, we present results showing the enhanced flaring that results when a minimum temperature is applied (such as might be expected under uniform external illumination) or when the disk is viewed at specific wavelengths. Results of this work are compared to recent *Hubble Space Telescope* observations of edge-on disk systems in § 5 and implications of these results for potential illumination of the disk by central star or FU Orionis outburst are summarized in § 6.

## 2. MODELS

We analyze the vertical and radial structure of a given viscously heated disk by calculating a radial series of one-dimensional vertical structure integrations. Axial symmetry is assumed. The mass flux, viscous efficiency, and stellar mass are taken to be constant for a given model, but the consequences of plausible variations are discussed. As long as the disk is geometrically thin, the radial diffusion of energy is negligible and a one-dimensional approximation is sufficient (Pringle 1981). In some of our higher mass flux models, the thickness ratio exceeds 0.1. Nevertheless, our qualitative conclusions are unchanged over most of the radial extent of the disk. The variables  $r$  and  $z$  are the radial and vertical coordinates, respectively. In the following,  $\Sigma$  and  $\dot{M}$  refer to the *full-plane* surface density and mass flux, respectively. The symbol  $\tau$  refers to the *half-plane* optical depth. With the subscript R, i.e.,  $\tau_R$ , a Rosseland mean optical depth is implied; in all other cases, the wavelength in microns will be explicitly stated:  $\tau_\lambda$ . The subscript  $m$  refers to midplane values. When the temperature variable  $T$  has no subscript, a local value is implied. The subscript  $e$  refers to values at the effective photosphere where  $\tau_R = \frac{2}{3}$ . The Keplerian orbital frequency,  $\Omega$ , is assumed to be the same at all heights in an annulus. Models are calculated varying the parameters  $\dot{M}$ ,  $\alpha$ ,  $M_*$ , and ambient temperature  $T_{\text{amb}}$ .

Calculation of the vertical structure is split into two parts at a transition optical depth:  $\tau_R = \tau_0$ . (The use of the Rosseland mean opacity even in optically thin regions

TABLE 2

ANALYTIC ROSSELAND MEAN OPACITY IN ( $\text{cm}^2 \text{ g}^{-1}$ ):  $\kappa = \kappa_n \rho^{\alpha_n} T^{\beta_n}$ .

$n$	$\kappa_n$	$\alpha_n$	$\beta_n$	Max. Temp. (K)	Reference
1.....	$1 \times 10^{-4}$	0	2.1	132	HS
2.....	$3 \times 10^0$	0	-0.01	170	HS
3.....	$1 \times 10^{-2}$	0	1.1	375	HS
4.....	$5 \times 10^4$	0	-1.5	390	HS
5.....	$1 \times 10^{-1}$	0	0.7	580	HS
6.....	$2 \times 10^{15}$	0	-5.2	680	HS
7.....	$2 \times 10^{-2}$	0	0.8	960 <sup>a</sup>	HS
8.....	$2 \times 10^{81}$	1	-24	1570 <sup>a</sup>	BL
9.....	$1 \times 10^{-8}$	2/3	3	3730 <sup>a</sup>	BL

<sup>a</sup> Transition temperatures are found by setting  $\kappa_n \rho^{\alpha_n} T^{\beta_n} = \kappa_{n+1} \rho^{\alpha_{n+1}} T^{\beta_{n+1}}$  and solving for  $T$ . These values require specification of  $\rho$ ; we use  $\rho = 10^{-9} \text{ g cm}^{-3}$ . The density dependence is weak; its exponent is given by  $(\alpha_{n+1} - \alpha_n)/(\beta_n - \beta_{n+1})$  and is, respectively, 0.0403, 0.0123, and 0.0476 for  $n = 7, 8$ , and 9.

where the Planck mean is more appropriate is justified by the closeness of the two values in the temperature and density regime used; Pollack et al. 1994). Integration first proceeds inward from  $\tau_0$  to the midplane. This calculation includes energy generation and the possibility of convective transport. The second calculation (when needed) proceeds vertically upward from the  $\tau_0$  surface and includes neither energy generation nor convection. Both models use the full gravitational term in the hydrostatic equation, which does not assume  $H \ll r$ :

$$\frac{\partial P}{\partial z} = -\rho g = \frac{-\rho G M_* z}{(r^2 + z^2)^{3/2}}, \quad (5)$$

where  $P$ ,  $\rho$ , and  $g$  are, respectively, pressure, density, and acceleration due to the gravity of the central star. Our technique of using a radial series of one-dimensional models does not allow the inclusion of the effects of radial transport of energy, which should only be important in the thickest of disks calculated here where  $H \rightarrow r$  (e.g., Pringle 1981).

We first discuss the inward integration. Viscosity is given by the “local” value,  $\nu(z) = \alpha_s c_s^2 / \Omega$ , where  $c_s^2 = P/\rho$  is the isothermal sound speed. The calculation begins at optical depth  $\tau_0$  with the surface temperature  $T_{\text{acc}}$  due to locally generated energy from equation (1). Density at the surface is found from the assumption of pressure balance. Starting from a guess of the Rosseland mean photospheric thickness,  $H_R$ , temperature and pressure are integrated inward using the flux-limited diffusion of energy plus mixing length convection and the hydrostatic equation (eq. [5]). The photospheric thickness is repeatedly modified until a solution is found in which the flux vanishes at the midplane. Surface density and midplane temperature are therefore found self-

TABLE 3

FREQUENCY-DEPENDENT OPACITIES ( $\text{g cm}^{-2}$ )

WAVELENGTH ( $\mu\text{m}$ )	APPROPRIATE TEMPERATURE RANGE (K)		
	0–225	260–580	680–1200
0.66 .....	72	58	23
2.2 .....	28	23	8.6
10 .....	16	14	10
60 .....	1.5	0.78	0.25
100 .....	0.38	0.28	0.086
350 .....	0.032	0.025	0.0085
1000 .....	0.0017	0.012	0.00085

consistently from the calculation. Full details of this calculation are given in Bell & Lin (1994). Modifications are made to account for the possibility of uniform external illumination. The temperature at the  $\tau_R = \frac{2}{3}$  surface of an irradiated annulus is increased from the accretion value (eq. [1]) such that  $T_e^4 = T_{\text{acc}}^4 + T_{\text{amb}}^4$ . The net flux of the annulus, however, represents only the locally generated flux and remains equal to the accretion flux:  $F_e = F_{\text{acc}} \equiv \sigma_B T_{\text{acc}}^4$ . Temperature and flux at the boundary of the calculation are found from these quantities depending on the value of  $\tau_0$ .

We consider two values of  $\tau_0$ . For the calculation of midplane conditions (§ 3), we first take  $\tau_0 = 0.03$ . The status of the atmosphere for this purpose is important only as the disk optical depth decreases below  $\frac{2}{3}$ . For the model calculations of midplane temperatures only the inward calculation is performed. The boundary conditions at the  $\tau_0$  surface in this case are modified from what was derived above for the  $\tau_R = \frac{2}{3}$  surface as follows. Viscous energy generation in the rarefied atmosphere is assumed to be negligible: We take  $F_0 = F_e$ . Temperature at the top of the grid:  $T_0$ , is the flux sum of the ambient temperature,  $T_{\text{amb}}$ , and the local accretion temperature,  $T_{\text{acc}}$ , as modified according to the Eddington approximation:  $T_0^4 = T_{\text{amb}}^4 + (3/4)T_{\text{acc}}^4[\tau_0 + f(\tau_0)]$ , where  $f(\tau_0)$  is the Hopf function, which equals 0.601242 for  $\tau_0 = 0.03$  (Mihalas 1978). When considering the disk thickness as a function of wavelength (§ 4) the details of the optically thin atmosphere on top of the disk are quite important. In this second case, we take  $\tau_0 = \frac{2}{3}$  and splice together inward and outward integrations. Temperature and flux at  $\tau_0$  are here given simply by  $T_0 = T_e$  and  $F_0 = F_e$ .

The optically thin atmosphere on top of the Rosseland mean photosphere is calculated with a separate procedure in which the full equation of hydrostatic equilibrium (eq. [5]) is explicitly integrated outward beginning from the temperature,  $T_e$ , and volume density,  $\rho_e$ , found at the outer boundary of the optically thick routine. The temperature in the atmosphere is allowed to drop no lower than  $T_{\text{amb}}$ . Radiation transport in the atmosphere (as elsewhere) is constrained by the principles of flux-limited diffusion (Levermore & Pomraning 1981; Bodenheimer et al. 1990). The atmosphere profiles generated using the two different methods are nearly indistinguishable. The explicit outward integration is used (1) to allow calculation to extremely low optical depths and (2) to restrict viscous energy generation to the optically thick layers of the disk.

Rosseland mean opacities are given by  $\kappa = \kappa_n \rho^{\alpha_n} T^{\beta_n}$  using the analytic formulae for iron poor opacities in Henning & Stognienko (1996, hereafter HS) at temperatures where dust particles exist, and formulae given in Bell & Lin (1994, hereafter BL) at hotter temperatures.<sup>2</sup> Because analytic formulae in ensuing sections explicitly use the temperature dependence of the opacity, we present the relevant exponents along with transition temperature in Table 2. HS opacities include olivine, orthopyroxene, volatile and refractory organics, water ice, troilite, and metallic iron as major grain species. We use their results for an iron poor grain mix. Frequency-dependent opacities were taken from the web site Henning & Stognienko (1997) as calculated for

<sup>2</sup> For clarity, the subscripts on the exponents  $\alpha$  and  $\beta$  will generally be omitted; exponents are assumed to be appropriate for the given temperature regime identified by  $n$ .

iron poor, homogeneous spheres. For a given frequency, these opacities are independent of temperature throughout a “plateau” regime where a particular mix of grain species exists. For comparison to other work, representative values taken from the detailed computer table that have been used in this work are given in Table 3 along with the approximate appropriate temperature ranges of the plateaus.

### 3. MIDPLANE CONDITIONS

Numerical results for midplane temperature, photospheric thickness, optical depth, and other disk properties are presented in this section. In the following subsections, these results are compared with approximate analytic formulae.

The top panel of Figure 1 shows the radial distribution of  $T_m$  and  $T_e$  for five constant mass flux models:  $\log_{10}(\dot{M}) = -9, -8, -7, -6, -5$  in  $M_\odot \text{ yr}^{-1}$ , for a fixed value of the viscous efficiency,  $\alpha_s = 0.01$ . The effective temperature is represented by dotted lines in Figure 1. Mass flux increases from bottom to top in both panels. Radial distribution of surface density is shown in the bottom panel; note that its radial dependence is far from a simple power law. We will

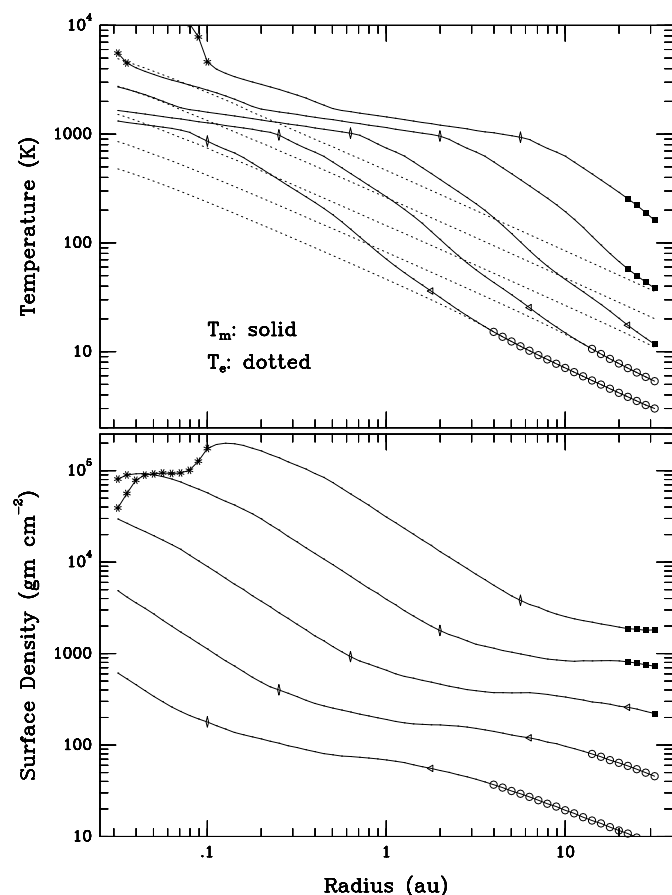


FIG. 1.—Results for vertical structure models for  $\dot{M} = 10^{-9}, -8, -7, -6, -5 M_\odot \text{ yr}^{-1}$ ;  $\alpha_s = 0.01$ ; mass flux increases from bottom to top. (top) Solid lines, midplane temperature; dotted lines, surface temperature. (bottom) Full plane surface density in  $\text{g cm}^{-2}$ . Narrow diamonds indicate the peak in relative, Rosseland mean disk thickness  $H_R/r$ ; beyond this radius, annuli are in shadow. Triangles indicate peak in absolute photospheric thickness  $H_R$ . Open circles indicate models for which the half plane Rosseland mean optical depth is less than  $2/3$ ; filled squares indicate a Toomre  $Q$ -value of less than 1. Stars indicate models where hydrogen is ionized and so are expected to be subject to thermal instability; these points are not shown in subsequent plots.

show that temperature and surface density profiles are governed by the local form of the opacity. Symbols at the radial extremities represent regions in which our assumptions may be expected to fail because the disks become either optically thin (circles) or are subject to gravitational instability (filled squares), or thermal instability (stars; these last models are not shown in subsequent plots). Narrow diamonds represent the maximum in the relative photospheric thickness  $H_R/r$  for a given constant  $\dot{M}$  model. Beyond this point, the disk will be mainly in shadow; in § 4.2 we find nearly the same radius for the peak in  $H_\lambda/r$  for wavelengths corresponding to the radiation of the star. Leftward pointing triangles indicate the maximum in absolute disk thickness. Note the narrow range of the midplane temperatures within which the narrow diamonds fall for all five models: We will show that this effect is caused by the temperature dependence of the opacity.

The radial dependence of photospheric disk thickness,  $H_R$ , is shown in Figure 2 for the same models. In the top panel, relative disk thickness  $H_R/r$  is shown in a log-log plot. Also shown are dotted lines indicating the local pressure scale height of each annulus estimated from midplane conditions. In the bottom panel,  $H_R$  vs.  $r$  is shown in “real space” coordinates with linear, equally spaced axes. Symbols are as before. Note the relatively small radius at which each of the models turns over in relative thickness and the small radius at which low mass flux models become optically thin to their own radiation. At the maximum  $H_R/r$  in the  $\dot{M} = 10^{-5} M_\odot \text{ yr}^{-1}$  disk, the angle, as seen from the

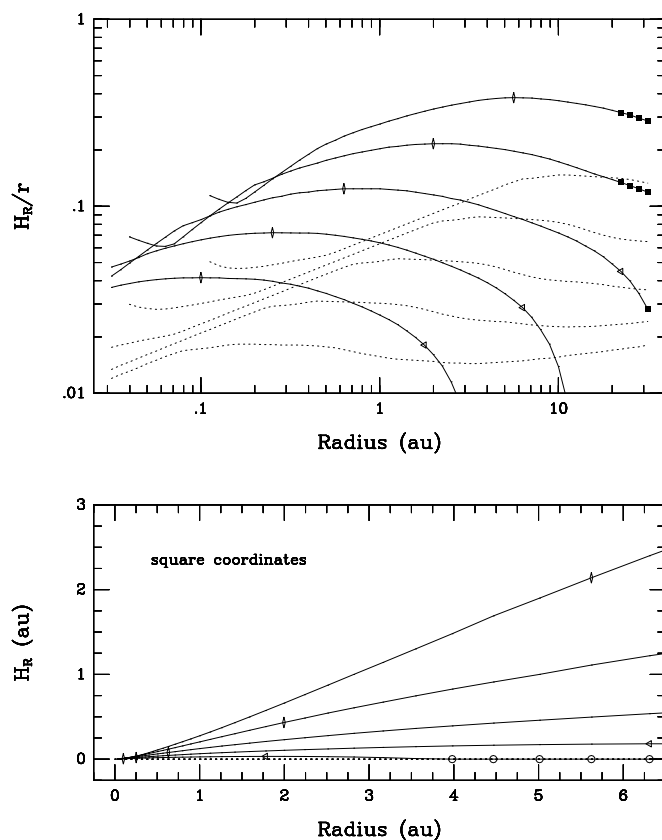


FIG. 2.—Variation of thickness of Rosseland mean disk photosphere with radius;  $\dot{M}$ 's and points as in Fig. 1. (a) Relative disk thickness:  $H_R/r$ . Dotted lines indicate the midplane relative pressure scale height,  $c_s/\Omega$ . Peak marked by narrow diamonds. (b) Absolute disk thickness,  $H_R$ , shown in square coordinates.

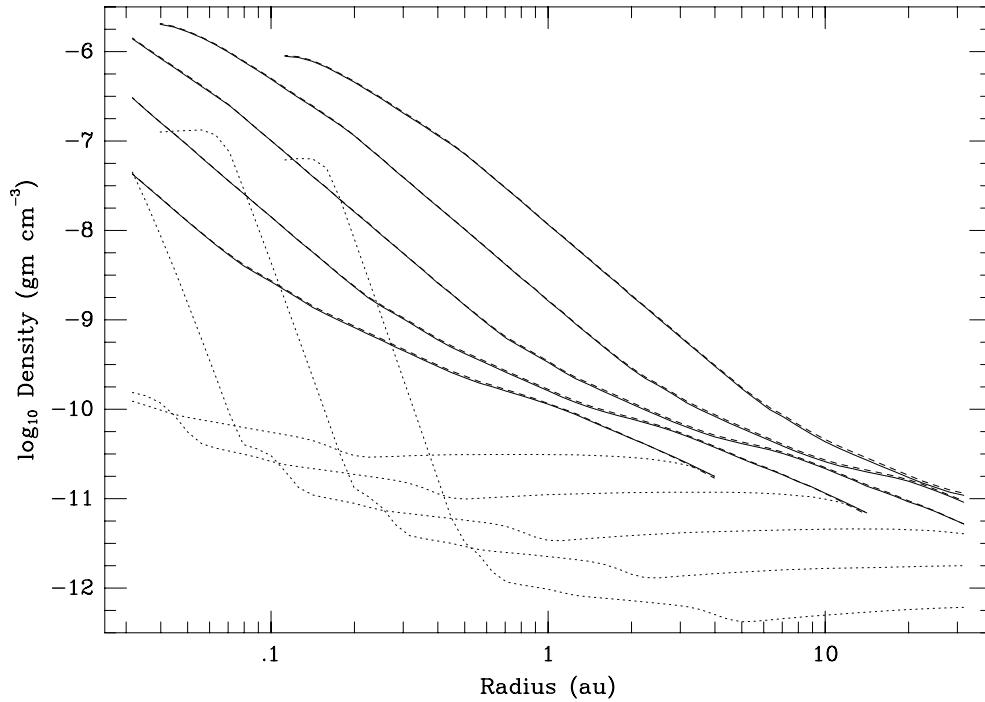


FIG. 3.—Volume density in disk at midplane (*solid lines*), at disk photosphere (*dotted lines*), and as estimated in text (*dashed lines*: almost coincident with solid). Mass fluxes as in Fig. 1: higher mass flux models have higher densities at the midplane and lower densities at the photosphere than do lower mass flux models over most of the radial extent. Optically thin models are not shown.

star, from disk midplane to photosphere is  $21^\circ$ ; about one third of the star's field of view is therefore occulted by the disk. In the lowest mass flux model, where  $\dot{M} = 10^{-9} M_\odot \text{ yr}^{-1}$ , the peak in  $H_R/r$  corresponds to a thickness of only  $0.9 R_\odot$  (an angle from midplane to photosphere as seen from the star of  $2.4^\circ$ ); the peak in  $H_R$  occurs at 1.8 au and is  $7 R_\odot$  (just over  $1^\circ$ ). Out to a radius of almost 2 au, the lowest mass flux disks are essentially flat and will therefore reprocess energy at the flat disk rate (eq. [3]).

In Figure 3 is shown the range of volume densities for the five standard models. Solid lines indicate midplane values, dotted lines indicate densities at the  $\tau_R = \frac{2}{3}$  surface. Dashed lines represent estimates of midplane densities given by  $\rho_m \approx \Sigma / [h_{\text{iso}}(\pi)^{1/2}]$ , where  $h_{\text{iso}}$  is the isothermal pressure scale height, which is  $2^{1/2} c_s / \Omega$ . If midplane sound speed and surface density are therefore specified, an accurate estimate of midplane volume density can be made:

$$\rho_m \approx \frac{\Sigma \Omega}{c_s \sqrt{2\pi}}. \quad (6)$$

In Figure 4 the photospheric thicknesses for  $\alpha_s = 10^{-2}$  (dotted lines) are compared with those for a smaller value of  $\alpha_s = 10^{-4}$ , the latter value is suggested by timescale fitting of FU Orionis outbursts (Kawazoe & Mineshige 1993; BL). While the shadow radius moves out only slightly, peaks in  $H_R/r$  increase by nearly a factor of 2 in low  $\alpha_s$  models. Filled squares, as in previous figures, indicate a Toomre  $Q$ -value of less than one. This parameter is a measure of susceptibility to local gravitational instability (Toomre 1964):

$$Q \equiv \frac{c_s \kappa}{\pi G \Sigma}, \quad (7)$$

where  $\kappa$ , the epicyclic frequency, equals  $\Omega$  in non-self-

gravitating disks. When  $Q$  drops below one, the disk becomes subject to axisymmetric fragmentation. Detailed numerical calculations suggest that nonaxisymmetric spiral disturbances may even occur for  $Q$  in the range 2–3 (Adams, Ruden, & Shu 1989; Tomley, Cassen, & Steinman-Cameron 1991). At radii designated with filled symbols, energy and angular momentum transport by density waves may invalidate the  $\alpha$  parameterization and the assumption of local energy dissipation.

The effect on the relative disk thickness of varying the gravitational point mass,  $M_*$ , is shown in Figure 5. Dotted lines indicate one-half solar mass, dashed lines, one solar

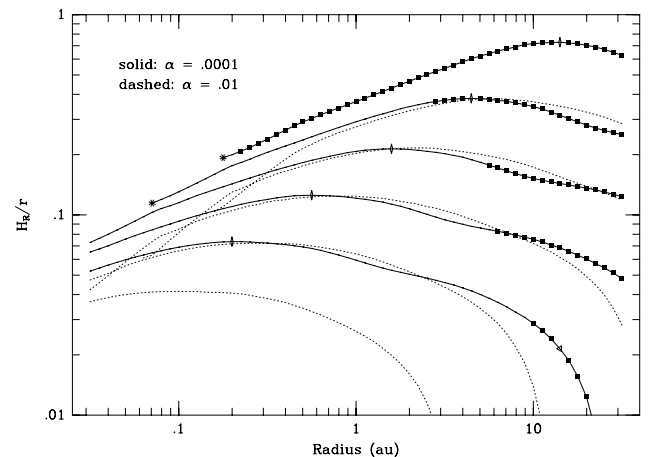


FIG. 4.—Relative disk thickness:  $H_R/r$ , for  $\alpha_s = 0.0001$  (*solid lines*) compared to standard 0.01 (*dashed lines*);  $\dot{M}$  increases from bottom to top. Points are as in Fig. 1. Radius of shadowing increases somewhat with reduced viscous efficiency; magnitude increases by factor of  $\approx 2$ . Notice that radius at which Toomre  $Q$ -value drops below one (marked by squares) moves significantly inward (compare Fig. 2).

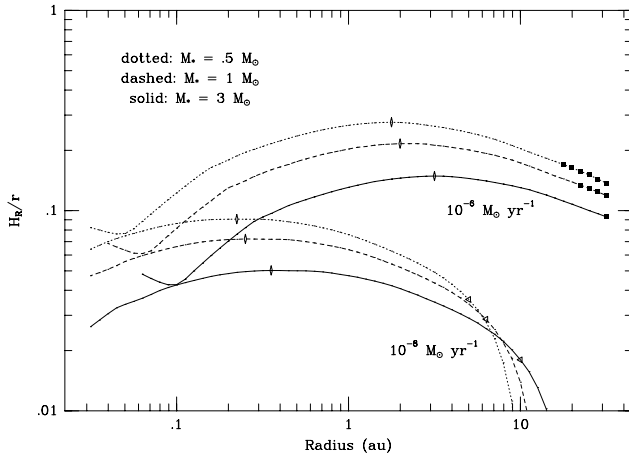


FIG. 5.—Relative disk thickness:  $H_R/r$ , for  $M_* = \frac{1}{2}$  (dotted lines) and  $3 M_\odot$  (solid lines) compared to standard  $1 M_\odot$  (dashed lines);  $\dot{M}$ 's are as marked and points are as in Fig. 1. Shadowing radii (narrow diamonds) change slightly with stellar mass.

mass and solid lines, three solar masses. The lower family of curves represent models that have radially constant mass flux of  $10^{-8} M_\odot \text{ yr}^{-1}$ , while the upper curves have mass flux of  $10^{-6} M_\odot \text{ yr}^{-1}$ . It can be seen that higher stellar mass models peak at lower relative thicknesses at larger radii. They are also less prone to gravitational instability and remain optically thick to larger radii.

Integrating out to 30 au, disk masses for standard models ( $\alpha_s = 0.01$ ,  $M_* = 1 M_\odot$ ) range from  $5 \times 10^{-3} M_\odot$  at  $\dot{M} = 10^{-9} M_\odot \text{ yr}^{-1}$  to  $0.8 M_\odot$  for the massive  $10^{-5} M_\odot \text{ yr}^{-1}$  disk model. (Disk masses are about  $0.2 M_*$  at the radius where they become self-gravitating.) Disks around higher mass stars tend to be slightly more massive for a given mass flux but are considerably less prone to gravitational instability. All surface density distributions derived here are considerably shallower than  $r^{-2}$ , which, if extrapolated to larger radius, implies that the nebular mass will be dominated by matter in the outer disk. All of the models derived here, however, become either optically thin or self-gravitating within 30 au, so a discussion of global disk masses is inappropriate in this paper.

In the following subsections, these numerical results are discussed in terms of simple analytic expressions.

### 3.1. Optical Depth

While some form of energy dissipation may occur in optically thin parts of the disk, it is not obvious to these authors that the turbulence postulated in the Shakura & Sunyaev viscosity prescription would necessarily be sustained. We therefore do not consider models for which  $\tau_R < \frac{2}{3}$  (marked with circles in above figures) to be self-consistent. An estimate of the radius at which a given disk will become optically thin may be made as follows. Note that throughout this discussion “optically thin to its own radiation” (i.e., in the Rosseland mean) is implied. Optical depth at different wavelengths will be discussed in following sections.

The Rosseland mean optical depth to the midplane is given approximately by  $\kappa_m \Sigma/2$ . At temperatures for which dust is the dominant source of opacity ( $T \lesssim 1300 \text{ K}$ ), the density dependence of the opacity is negligible. Opacity can then be represented  $\kappa = \kappa_n T^\beta$ , where  $\kappa_n$  and  $\beta$  depend only on the local temperature. The full plane surface density at

large radius may be estimated from the steady viscous disk result:  $\dot{M} = 3\pi\Sigma\nu$ , with the assumption that mass flux is radially constant throughout the disk. Taking midplane sound speed:  $c_s^2 = R_g T_m/\mu$ , where  $R_g$  is the gas constant, and the mean molecular weight  $\mu = 2.3$  (appropriate for molecular regions), we derive the following approximate relations:

$$\Sigma \approx \frac{\dot{M}}{3\pi} \frac{\Omega}{\alpha_s c_s^2}; \quad (8)$$

$$\Sigma \approx 615 \text{ g cm}^{-2} \left( \frac{\dot{M}}{10^{-7} M_\odot \text{ yr}^{-1}} \right) \left( \frac{M_*}{1 M_\odot} \right)^{1/2} \times \left( \frac{\alpha_s}{0.01} \right)^{-1} \left( \frac{r}{1 \text{ au}} \right)^{-3/2} \left( \frac{T_m}{600 \text{ K}} \right)^{-1} \left( \frac{\mu}{2.3} \right). \quad (9)$$

This result is independent of the opacity but requires explicit specification of  $T_m$ .

Central temperature can be estimated from the diffusion approximation for a plane-parallel atmosphere with energy sources (Lin & Papaloizou 1985; Cassen 1994),  $T_m = T_e(3\tau_R/8)^{1/4}$ ; by the assumption of vertical thermal balance (eq. [1]), and by taking  $\rho \approx \rho_m \approx \Sigma/2h$  and  $h \approx c_s/\Omega$ :

$$T_m^{5-\beta+(3\alpha/2)} = \frac{3^{1-\alpha} \kappa_n}{2^{7+\alpha} \sigma_B} \left( \frac{\mu}{R_g} \right)^{1+(3\alpha/2)} \left( \frac{\dot{M}}{\pi} \right)^{2+\alpha} \times \alpha_s^{-(1+\alpha)} \left( \frac{GM_*}{r^3} \right)^{(3/2)+\alpha}; \quad (10)$$

$$\frac{d \ln T_m}{d \ln r} = -\frac{3}{2} \frac{(3+2\alpha)}{(5-\beta+3\alpha/2)}; \quad (11)$$

The latter equation is valid when mass flux, viscous efficiency, and molecular weight are held constant with radius. The exponent  $\alpha$  can be set to zero in cool regions where opacity is independent of density. When  $\beta = 2$  and  $\alpha = 0$ , this equation reduces to the Lin & Papaloizou (1985) expression  $T_m \propto r^{-3/2}$ . Large negative values of  $\beta$ , characteristic of transition regions where particles are being destroyed at the midplane, lead to a temperature that decreases only slowly with radius, close to radial isothermality. Temperatures range from only 1000 to 1600 K (corresponding to the boundaries of the  $n = 8$  opacity regime; Table 2) in over an order of magnitude in radius in our models as shown in Figure 1 (see also Morfill & Wood 1989; Boss 1993; Cassen 1994).

Values derived from this equation are compared to numerically derived midplane temperatures for a  $\dot{M} = 10^{-7} M_\odot \text{ yr}^{-1}$  disk in two cases: where  $\alpha_s = 10^{-2}$  and  $10^{-4}$  in Figure 6. It can be seen that excellent agreement occurs for the larger value of  $\alpha_s$  and tolerable agreement for the smaller. Note that better agreement in the hottest regime (law 9) could probably have been obtained by modifying the mean molecular weight from its fixed value of 2.3. Taking equation (8) and keeping  $\dot{M}$ ,  $\alpha_s$ , and  $\mu$  constant, we get  $\Sigma \propto (r^{3/2} T_m)^{-1}$ , which from equation (11), can be expanded to

$$\frac{d \ln \Sigma}{d \ln r} = -\frac{3}{2} \frac{(2-\beta-\alpha/2)}{(5-\beta+3\alpha/2)}. \quad (12)$$

This estimate gives a constant surface density in the outer regions where  $\beta = 2$  and  $\alpha = 0$ , in agreement with the ten-

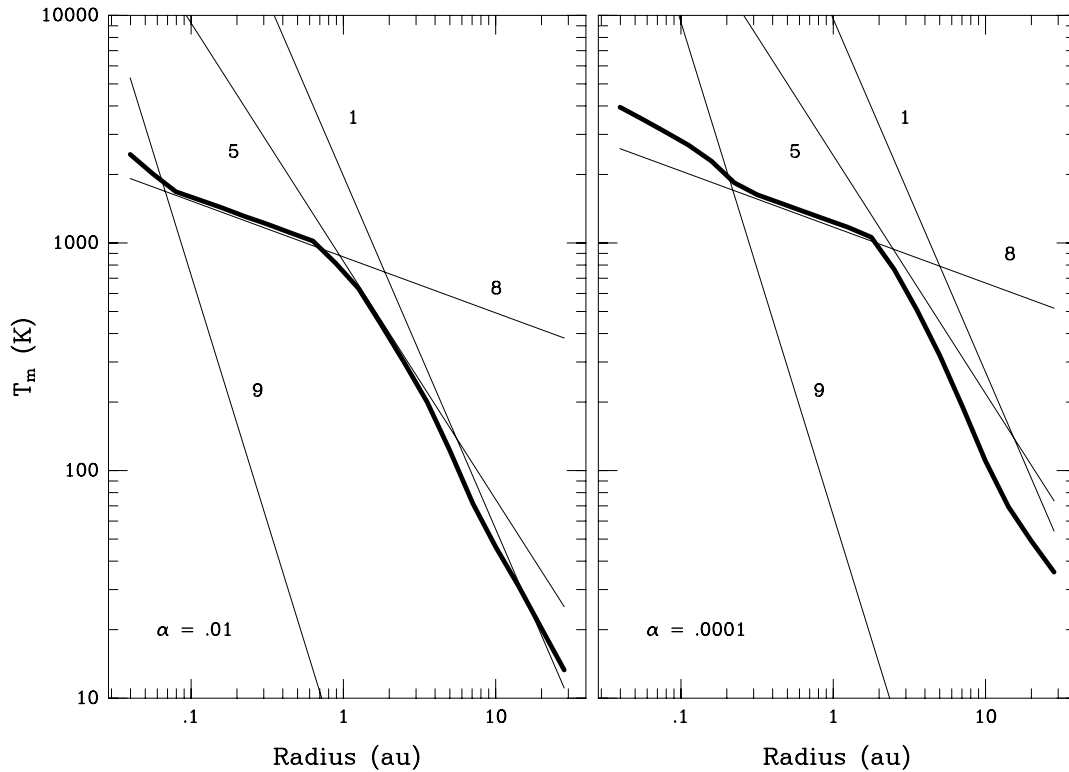


FIG. 6.—Midplane temperature for  $\dot{M} = 10^{-7} M_{\odot} \text{ yr}^{-1}$  model for (left)  $\alpha_s = 0.01$  and (right)  $\alpha_s = 0.0001$ . Numerical calculations (heavy line) and as calculated evaluating eq. (10) with various opacity laws over the entire radial range (thin lines: numbers correspond to opacity regimes in Table 2). For clarity, only selected opacity laws are shown, other laws show similar close fit in appropriate temperature regimes.

dency seen in the bottom panel of Figure 1 at radii beyond the peak in  $H_R/r$  and before the disk approaches isothermality and the diffusion approximation breaks down.

An expression for the optical depth can be similarly derived:

$$\tau_R^{5-\beta+(3\alpha/2)} = \frac{2^{2-6\beta+5\alpha}}{3^{6-2\beta+7\alpha}} \sigma_B^{1-\beta+(3\alpha/2)} \left\{ \frac{\kappa_n}{\alpha_s^{1+\alpha}} \left( \frac{\mu}{R_g} \right)^{1+(3\alpha/2)} \right\}^4 \times \left( \frac{\dot{M}}{\pi} \right)^2 \left( \frac{GM_* \dot{M}}{\pi r^3} \right)^{1+\beta+(5\alpha/2)}, \quad (13)$$

The radius at which the disk becomes optically thin,  $R_{(\tau_R=2/3)}$ , is found by setting  $\tau_R = \frac{2}{3}$  and solving the above equation for  $r$ . Assuming that the nebula becomes optically thin somewhere beyond the radius where ice grains condense ( $T \lesssim 160$  K), for which  $\kappa_n = 10^{-4}$ ,  $\beta \approx 2$ , and  $\mu = 2.3$ , these formulae can be evaluated:

$$\tau_R = 34 \left( \frac{\dot{M}}{10^{-7} M_{\odot} \text{ yr}^{-1}} \right)^{5/3} \left( \frac{\alpha_s}{0.01} \right)^{-4/3} \times \left( \frac{M_*}{1 M_{\odot}} \right) \left( \frac{r}{10 \text{ au}} \right)^{-3}, \quad (14)$$

$$R_{(\tau_R=2/3)} = 35 \text{ au} \left( \frac{\dot{M}}{10^{-7} M_{\odot} \text{ yr}^{-1}} \right)^{5/9} \times \left( \frac{\alpha_s}{0.01} \right)^{-4/9} \left( \frac{M_*}{1 M_{\odot}} \right)^{1/3}. \quad (15)$$

A summary of values derived from an analogous relation that uses  $\beta = 2.1$  is given in Table 4 for  $M_* = 1 M_{\odot}$ . In the

regions of overlap, these results are in substantial agreement with the results of the detailed vertical structure models (Figs. 1 and 4).

### 3.2. Convection

There is currently some question over the degree to which convection, driven by the dissipation of turbulent energy associated with angular momentum transport, can be self-sustaining in accretion disks. The linear analysis of Ryu & Goodman (1992) indicates that convection would produce a net transport of angular momentum inward, in the reverse direction of what would be needed to move mass inward through the nebula. This result is supported by the numerical calculations of Kley, Papaloizou, & Lin (1993), Cabot (1996), and Stone & Balbus (1996). Further, the weak convection expected in cool regions of the disk may be suppressed by radial streaming for  $\alpha_s \gtrsim 0.03$  (Kley et al. 1993;

TABLE 4  
RADIUS (IN AU) BEYOND WHICH DISKS  
BECOME OPTICALLY THIN (IN THE  
ROSSELAND MEAN) TO THEIR  
OWN RADIATION

$\dot{M}$ ( $M_{\odot} \text{ yr}^{-1}$ )	$\alpha_s$		
	$10^{-2}$	$10^{-3}$	$10^{-4}$
$10^{-9}$ .....	3.0	8.2	22
$10^{-8}$ .....	11	29	78
$10^{-7}$ .....	38	100	270
$10^{-6}$ .....	130	360	970
$10^{-5}$ .....	470	1300	3400



Różyczka, Bodenheimer, & Bell 1994). Nevertheless, mass accretion must be accompanied by some form of dissipation within the disk, and our vertical structure models indicate that such heating is capable of driving convection. The turbulence so produced may also be an important factor in the coagulation of particles and their subsequent growth into planetesimals. We therefore discuss its implications for the vertical structure of circumstellar disks.

The efficiency of convection throughout the radial extent of our five standard case models is illustrated in Figure 7. The ordinate represents the fraction of the total flux that is carried by convection, averaged over the height of the disk:

$$\text{Convective Transport} \equiv \frac{1}{H_R} \int_0^{H_R} \frac{F_{\text{con}}(z)}{F_{\text{tot}}(z)} dz, \quad (16)$$

and the abscissa represents the midplane temperature of the given model. The five lines indicate different mass flux models as in the previous figures. Vertical lines indicate particle destruction fronts (as in Table 2). Narrow diamonds demonstrate that the peak relative disk thickness coincides with the final dust destruction front at about 1000 K. Convective transport reaches a peak of about 20% for the highest mass flux models in the regions where ice grains exist throughout the vertical extent of the nebula ( $T_m \approx 100$  K). In this regime,  $\beta$  is at its maximum in the cold outer disk of  $\approx 2$ . Lower mass fluxes show smaller convective efficiencies in this region because of the decreased vertical optical depth. Convective efficiency decreases at tem-

peratures just above the ice grain destruction front (beginning at 130 K), then again rises in a broader peak that encompasses the next two fronts at 375 and 580 K. Efficiencies for all mass fluxes are comparable in this region where organics and dust grains dominate the opacity and  $\beta \approx 1$ .

Vertical structure calculations confirm that convection, even when present, does not greatly alter the temperature profile of the disk. Figure 8 shows an  $\alpha_s = 0.01$ ,  $\dot{M} = 10^{-7} M_\odot \text{ yr}^{-1}$  annulus with and without convection (heavy lines and light lines, respectively). The annulus is at 7 au near the peak of the convective region of the outer disk. It can be seen that even though nearly 20% of the flux is carried by convection (cf. Fig. 7,  $T_m \approx 70$  K), the temperature and density profiles of the two models are not greatly different. This is principally because the gradient  $\nabla(z) \equiv \partial \ln T / \partial \ln P$  (solid lines, upper right panel) is not greatly different between the two cases (see also Cassen 1993 for an analytic discussion). In solving the full mixing length equations, the gradient falls between radiative and convective values and remains superadiabatic throughout most of the vertical extent of the disk.

Recent two-dimensional disk simulations have suggested that it is not sufficient to satisfy the Schwarzschild criterion ( $\nabla > \nabla_{ad}$ ) for convection to occur (Kley et al. 1993; Różyczka et al. 1994). Strong radial pressure gradients cause a two-stream flow pattern in numerical simulations (outward along the midplane and inward near the surface) that overwhelms convective motions unless an additional

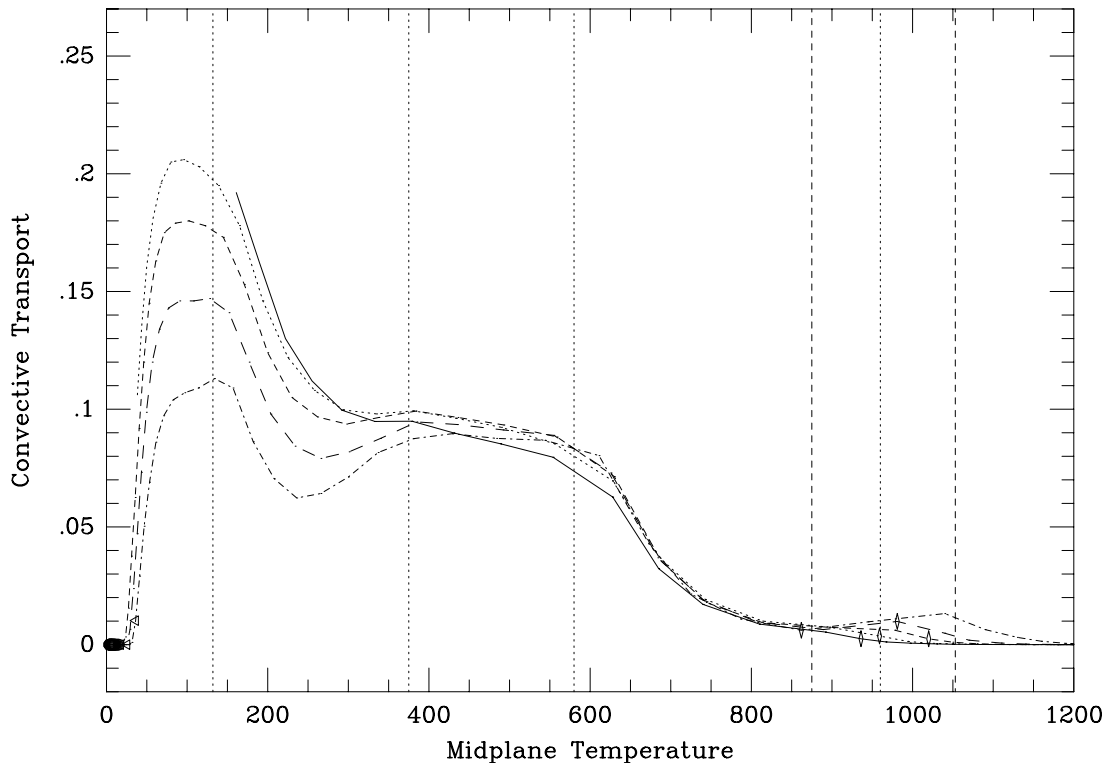


FIG. 7.—Radial distribution of convection. “Convective transport” is a vertically averaged measure of the fraction of flux transported by convection (eq. [16]). Each line represents a constant mass flux model; line types solid, dotted, short dashed, long dashed, and dot dashed represent models with, respectively,  $10^{-5}$ ,  $10^{-6}$ ,  $10^{-7}$ ,  $10^{-8}$ , and  $10^{-9} M_\odot \text{ yr}^{-1}$ . Symbols are as in Fig. 1. Vertical dotted lines mark the dust destruction fronts (“Max. Temp.” column of Table 2 of opacity regimes 1, 3, 5, and 7); the two vertical dashed lines indicate the temperature of the final dust destruction front varying the density an order of magnitude in either direction. The peak in  $H_R/r$  (narrow diamonds) coincides closely with this final dust destruction zone. The convective regions further out in the disk (i.e., at cooler temperatures) will be shielded from illumination by the central object.

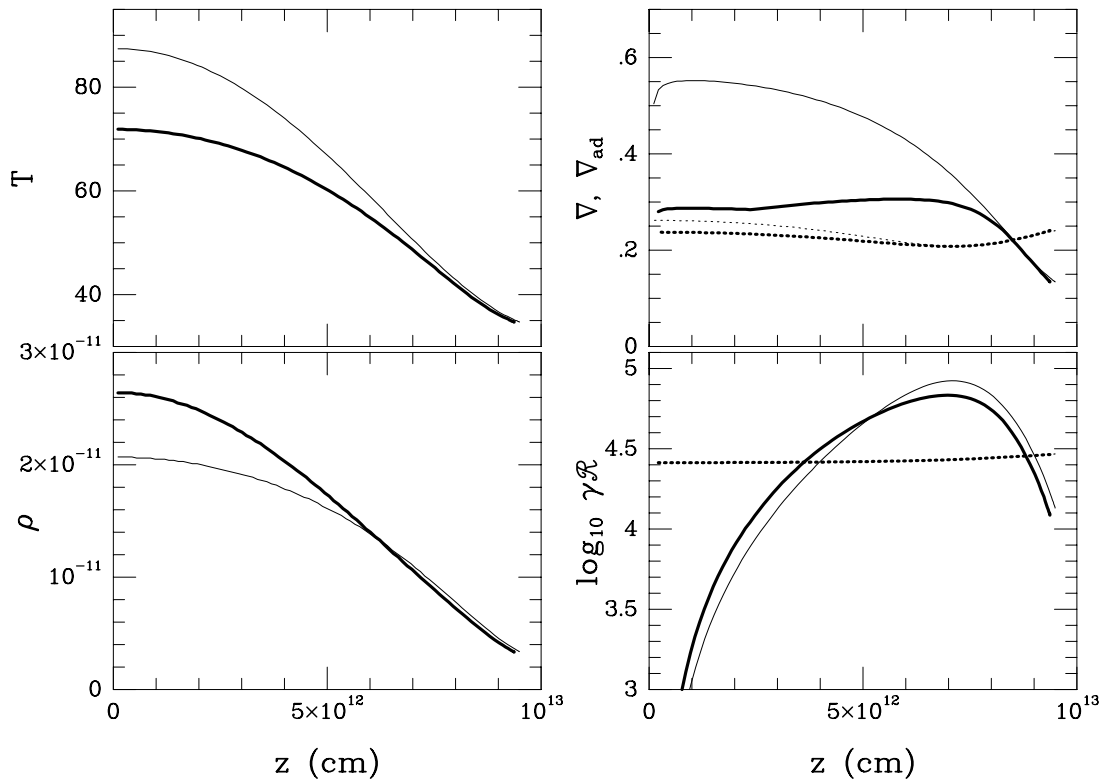


FIG. 8.—Annulus with  $\dot{M} = 10^{-7} M_{\odot} \text{ yr}^{-1}$  at 7 au showing vertical structure with convection (*heavy lines*) and without (*light lines*). In upper right panel, true gradients are solid; adiabatic gradients for the two models are dotted. Note the similarity of  $T$  and  $\rho$  for the models. In the lower right is shown a convective criterion discussed in the text.

criterion involving Rayleigh and Taylor numbers ( $\mathcal{R}$  and  $\mathcal{T}$ , respectively) is satisfied. Kley et al. (1993) carry out a linear stability analysis and conclude that for convection to occur, the following relationship must be met:

$$\gamma \mathcal{R} = \frac{-g \rho H_R^4}{\nu} \frac{3 \kappa \rho}{4 a c T^3} \frac{\partial s}{\partial z} > \frac{\mathcal{T}}{4(4\pi)^2} + (4\pi)^4, \quad (17)$$

where  $\gamma$  is the specific heat ratio and  $\mathcal{T} = (2\Omega H_R^2/\nu)^2$ . The entropy gradient may be given by  $\partial s/\partial z = -C_v \Omega^2 z \nabla \rho/P$ . This analysis is perhaps suspect in that the large-scale  $\alpha$ -law viscosity is used in this equation in place of the orders of magnitude smaller molecular viscosity for which the Rayleigh number was derived (Chandrasekhar 1961). In the lower right panel of Figure 8 we show that  $\gamma \mathcal{R}$  (*solid line*) exceeds the stability criterion in equation (17) (*dashed line*) throughout most of the vertical extent of the annulus. In general, because of our relatively small value of  $\alpha_s$ , where the Schwarzschild criterion is satisfied, so is equation (17).

In the special case in which the disk is homologously contracting toward the midplane, Lin & Papaloizou (1980) show that convection occurs when the opacity temperature exponent  $\beta$  exceeds  $(3\gamma - 4)/(\gamma - 1)$ , which equals  $\frac{1}{2}$  in molecular regions where the ratio of specific heats  $\gamma = 7/5$  (Ruden & Pollack 1991). We present a more general derivation in the Appendix and find a less restrictive criterion on  $\beta$  for the existence of convection. In either case, convection is strongly quenched for large negative values of  $\beta$ . It is shown that the criterion is somewhat complicated in the general case including energy generation by viscous dissipation. Convective regions in the cool outer disk occur beyond the

disk's peak in  $H_R/r$  and so will be shadowed by the inner disk from the central object. Convection in these regions will not be suppressed by stellar illumination. In conclusion, even if convection is not likely to be a factor for turbulent mass transport and does not greatly modify the vertical temperature profile, it may still be a common feature of internally heated disks.

#### 4. APPARENT DISK FLARING

In previous sections, we have summarized conditions at the disk midplane and described the disk shape as defined by the disk photosphere. In this section, we address the question “What do disks look like from the outside?” In § 4.1 we derive an analytic expression for the radial trend of disk scale height,  $h$ , as a function of opacity and show that these trends are reflected in the radial trends of the Rosseland mean photosphere:  $H_R$ . In § 4.2, we show that both  $H_R/r$  and  $H_R/r$  turn over and start to decrease at the same well defined radius. The *apparent* thickness of the disk (i.e., when viewed at a given wavelength) depends upon the opacity at the wavelength viewed: At shorter wavelengths the disk appears thicker, while at longer wavelengths it appears thinner until at 1 mm, all but the innermost annuli of the disk are transparent. In the third subsection, we show that embedding any of these disks in a warm radiation bath both increases apparent radial flaring and inhibits gravitational instability. In the outer disk where the ambient temperature is greater than the midplane temperature expected from viscous dissipation alone, the photosphere begins to flare strongly as  $r^{3/2}$  as appropriate for isothermal disks.

#### 4.1. Scale Height and Rosseland Mean Photosphere

It is clear from Figure 2 that, contrary to the usual assumption that disks flare at large radii, models show a maximum in  $H_R/r$  and begin to decrease at fairly modest radius. Although the scale height  $h$  (Fig. 2, *dashed lines*) is considerably smaller than the Rosseland mean photosphere (*solid lines*), both show similar radial trends and inflections. In the optically thick part of the disk, the scale height is typically thinner than the photosphere by more than a factor of 2, which is to say that the disk is two to three scale heights thick. Lower  $\alpha_s$  models may be three or more scale heights thick. The tendency for scale heights to peak at larger radii than disk photospheres can be understood in that the detailed calculations include temperatures cooler than  $T_m$ , and therefore begin to be governed by cooler opacity laws at smaller radii than do the scale heights, which are based solely on midplane values. At the outer radii, where the disks become more optically thin, trends in scale height and photosphere diverge, so the approximation  $H_R \sim h$  is no longer valid.

We use the pressure scale height to investigate photospheric trends, and show that, as with other nebular variables, it is the temperature exponent of the opacity that determines the radial trend of disk thickness. Pressure scale height depends on the midplane temperature (cf. eq. [4]):  $(h/r) \propto (T_m r)^{1/2}$ . Disks have been expected to flare (e.g., Kenyon & Hartmann 1987) based on the assumption that the midplane temperature scales with the surface temperature. For example, in a constant mass flux disk where  $T_e \propto r^{-3/4}$ , the scale height  $h$  increases modestly faster than radius as  $r^{9/8}$ . This approach amounts to neglecting the temperature dependence of the opacity. More properly (although still approximately) we take the radiative approximation for  $T_m$  from equation (10) and find

$$(h/r)_1 \propto r^{(1-2\beta-3\alpha)/(20-4\beta+6\alpha)} \approx r^{(1-2\beta)/(20-4\beta)}. \quad (18)$$

Since  $\beta < 5$  in the relevant opacity regimes, the disk flares ( $h/r$  increases with radius) for  $\beta < \frac{1}{2}$  and does not flare for  $\beta > \frac{1}{2}$ . Thus, in the cold outer disk where  $\beta \approx 2$ , the disk does not flare but rather decreases in relative scale height with radius. By implication, the relative photospheric thickness  $H_R/r$  of optically thick disks therefore also decreases with radius.

In the derivation of the above expression, the surface density was constrained by the steady viscous disk result (eq. [8]) with constant  $\alpha_s$ . A derivation that retains the explicit dependence on surface density has the advantage of eliminating the implicit dependence on viscous efficiency; it assumes only that  $T_e \sim r^{-3/4}$ . For the radial trend in this case, we find

$$(h/r)_2 \propto r^{(1-\beta-\alpha)/(8-2\beta+\alpha)\Sigma^{1/(8-2\beta+\alpha)}} \approx r^{(1-\beta)/(8-2\beta)\Sigma^{1/(8-2\beta)}}. \quad (19)$$

If the surface density is constant with radius, the critical value of  $\beta$  increases from  $\frac{1}{2}$  to 1. If the surface density decreases with radius, the critical value of  $\beta$  is decreased. Only if the surface density increases with radius faster than  $r$  can the disk be made to flare when  $\beta = 2$ . It is therefore unlikely that constant mass flux disks in which the only heating source is due to local dissipation increase in thickness indefinitely. It can be seen from Figures 1 and 7 that

the peak in  $H_R/r$  for all of our models occurs at a  $T_m$  of just under 1000 K. This temperature corresponds (Table 2) to the onset of dust grain formation in the nebula. When dust grains dominate the opacity, the temperature dependence of the opacity increases above the critical value of  $\beta$  derived above, and the disk turns concave down. Note that the disk remains tilted away from the central object even though the opacity passes through several regimes with negative  $\beta$  ( $n = 2, 4$ , and  $6$  in Table 2). This is due principally to the narrow temperature range over which each relevant grain species is destroyed (see the fifth column). The dependence of disk shape on the local opacity exponent also governs the complicated structure of the luminous inner disk during FU Orionis outburst (e.g., Turner, Bodenheimer, & Bell 1997). Where hydrogen is ionized and the opacity decreases with temperature:  $T_m > 10^4$  K, the disk increases dramatically in relative thickness over a small radial extent (the “volcano region” in Turner et al. 1997). Outside of this region, there is a rapid decrease in disk thickness caused by a regime dominated by  $H^-$  opacity in which opacity increases strongly with temperature  $\kappa \propto T^{10}$ .

As particles coagulate to form larger objects, both the opacity and its temperature dependence ( $\beta$ ) decrease (Mucha 1996; Schmitt, Henning, & Mucha 1997). This will lead to a disk that does flare with radius. It may be that during the early stages of particle growth in the solar nebula, the outer disk was shielded by radiation from the central object, but at later times, as the opacity diminished and became independent of the local temperature, the material in the dissipating disk became exposed to warming by the young Sun.

#### 4.2. Wavelength-dependent Photosphere

The  $\tau_\lambda = \frac{2}{3}$  surfaces for a given mass flux model are found by integrating  $\kappa_\lambda \rho dz$  inward through a given disk atmosphere. The Henning and Stognienko frequency-dependent opacities,  $\kappa_\lambda$ , as summarized in Table 3 are used. These opacities were developed specifically for protoplanetary accretion disks and include the influence of dust aggregates. Frequency-dependent opacities in this regime are independent of density (except in that sublimation temperatures are density dependent). Each of the seven grain species included in the calculation has an opacity independent of temperature. At the coldest temperatures, all species are present and opacity is highest. As each species is thermally destroyed, it ceases to contribute to the overall opacity and its effect is removed from the calculation. The opacity of a given combination of grain species is therefore independent of temperature. Disk surfaces are found by integrating  $\kappa \rho dz$  inward through the atmospheres of disk models with the frequency-dependent opacity appropriate for the local temperature for a given frequency.

Typical resulting disk shapes are shown in the upper left panel of Figure 9 for a disk with mass flux  $10^{-6} M_\odot \text{ yr}^{-1}$  as seen at  $\lambda\lambda = 0.66, 2.2, 60, 100, 350$ , and  $1000 \mu\text{m}$ . All but the millimeter surface show peaks in relative thickness at about the same radius; the shadow radius as determined from the Rosseland mean photosphere is therefore approximately correct for radiation of all wavelengths. Beyond its peak,  $H_\lambda/r$  decreases more slowly with radius than  $H_R/r$ . At the outer radii,  $H_\lambda/r$  for short wavelengths begins to increase again. Even at the shortest wavelength ( $6600 \text{ \AA}$ ) where the effect is most pronounced, at 100 au the relative thickness has not yet increased over the maximum in the disk at a few

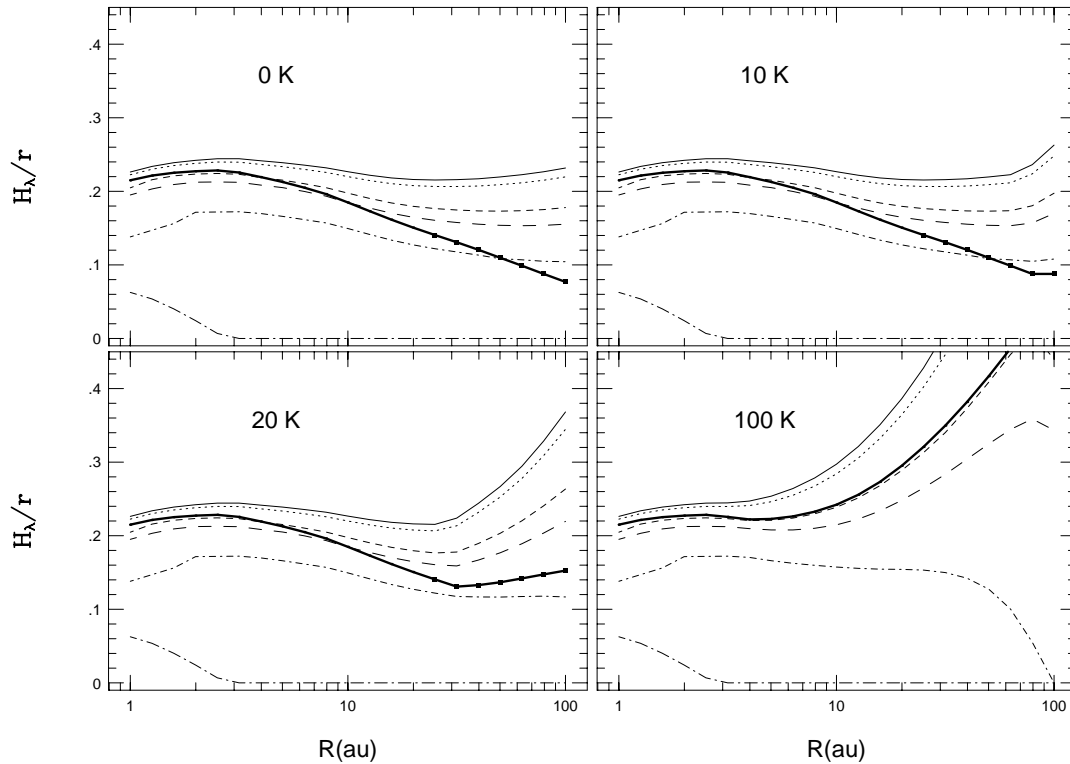


FIG. 9.—Radial distribution of relative disk thickness for  $\dot{M} = 10^{-6} M_{\odot} \text{ yr}^{-1}$  disk with minimum temperature as marked observed in the Rosseland mean and at various wavelengths. The heavy line in each panel indicates the relative thickness of the Rosseland mean relative photosphere. Other lines indicate photospheres as seen at different wavelengths; from the top down  $\lambda\lambda = 0.66, 2.2, 60, 100, 350$ , and  $1000 \mu\text{m}$ .

au, i.e., the outer disk is still shielded by the inner disk from radiation emitted by the central object. A planet-forming region between 2 and 50 au is therefore shadowed from most of the central object radiation for this mass flux model. For lower mass fluxes, the shadow radius falls at even smaller radii. It can be seen that millimeter-wavelength radiation has such a low opacity that it passes through the entire disk thickness at most radii of this rather high mass flux disk. Low mass disks are transparent at all radii to mm radiation, but the innermost annuli of higher mass disks ( $r \lesssim 2$  au for this disk) are not transparent to this radiation. Disk masses determined by total mm fluxes (as in Beckwith et al. 1990) will not be sensitive to mass in this region and should be regarded as lower limits.

#### 4.3. Embedded Disks

As shown in § 1, even viscously active accretion disks become dominated by ambient cloud conditions in their outer regions. For low mass flux, this could occur as close to the star as 1–10 au (see Fig. 1). The remaining three panels of Figure 9 show the impact on local disk structure of limiting the minimum temperature to 10, 20, and 100 K. At some radius, this external illumination drives the disk to vertical isothermality. The radius at which this occurs for any given model and ambient temperature can be estimated from the temperature profiles in Figure 1.

An ambient radiation temperature of 10 or 20 K is typical of quiet molecular clouds such as the Taurus and Ophiucus regions. In both of these cases, flaring is increased in the outer disk, but there still remains a shadowed region between a few and forty au. In the hottest case, where

$T_{\text{amb}} = 100$  K, this shadowed region is at last eliminated and all radii of the disk are exposed to radiation from the central object. With such an intense external field, however, the central object would have to be very luminous to compete with background radiation as a source of illumination.

In the heavy curves representing the Rosseland mean photosphere, annuli with Toomre  $Q$ -values less than one are indicated by filled squares. In the first three panels, the disk becomes subject to gravitational instability within thirty au. Under extreme external illumination, as represented by the 100 K radiation field in the final panel, surface density in a constant mass flux disk is decreased and this instability is suppressed (see also d'Alessio et al. 1997). Disks forming in hot regions such as the Orion Nebula might therefore evolve with significantly different processes than disks in colder environments.

#### 5. DISCUSSION

While only several years ago the prospect of directly observing the inner planet-forming disk ( $r \lesssim 40$  au) seemed remote, recent developments suggest we may be approaching this ideal. Some of the highest spatial resolution techniques to date have been used to probe the envelope/disk structure around young protostar HL Tau. Adaptive optics images of HL Tau taken at  $H$ ,  $J$ , and  $K'$  resolve a 150 au radius disk (Close et al. 1997) and confirm previous detections of the HL Tau disk by submillimeter (0.8 mm; Lay et al. 1994) and millimeter (2.7 mm; Mundy et al. 1996) interferometry. This system seems to be still embedded in a dusty circumstellar envelope that surrounds the dense disk (e.g.,

*Hubble Space Telescope* observations by Stapelfeldt et al. 1995) so is not an ideal candidate for testing the disk structure models put forth in this paper (for a detailed discussion of this object see Men'shchikov, Henning, & Fischer 1997). In this section we discuss some observations of more isolated disks as seen in the optical with the *Hubble Space Telescope* (*HST*) with sizes of a few hundred au in radius. Because edge-on systems present more material along lines of sight near the disk midplane than other systems, they are detectable to greater radii. Here we briefly discuss two recent *HST* observations of edge-on disks that bear on the issue of shape.

Burrows et al. (1996, hereafter Betal) constrain the density profile in the HH30 system by comparing the observed *I* band *HST* image of this nearly edge-on system to images simulated by Monte Carlo scattering calculations. A uniform flaring of the density scale height as  $h \propto r^{1.45}$  out to a radial distance of 250 au is derived. Notice that a scale height rather than a photospheric thickness is being defined. The observable disk mass is only  $4 \times 10^{-4} M_{\odot}$ , and their model disk is (vertically) optically thick to its own radiation out to only 2.7 au from the central object. This is very close to the  $h \propto r^{1.5}$  expected from an isothermal disk, the condition expected in regions where background radiation dominates over local energy production. Betal use a Gaussian vertical density profile that automatically has the same structure as a hydrostatic, isothermal disk atmosphere (Pringle 1981). The reference scale height of 15.5 au at a distance of 100 au, derived by Betal, requires a background temperature of 30 K to be supported against the potential of a  $0.5 M_{\odot}$  central star. Thus, the Betal observed disk structure is plausibly determined solely by a uniform background radiation field. Their derived midplane density profile of  $\rho_m \propto r^{-2.2}$  corresponds (with their scale height) to a surface density that scales as  $\Sigma \propto \rho_m h \propto r^{-3/4}$ . This is flatter than the commonly used value (e.g., Beckwith et al. 1990) derived from the minimum mass solar nebula estimate of  $\Sigma \propto r^{-3/2}$  but steeper than what is derived for thin disks formed from rotating clouds of varying initial density distributions under the assumption of conservation of angular momentum on collapse:  $\rho_m \propto r^{-1}$  to  $r^{-7/4}$  (Stemwedel et al. 1990), which correspond to  $\Sigma \propto r^{1/2}$  to  $r^{-1/4}$  for an isothermal disk.

It should be mentioned that the presence of micron-sized dust at high altitudes with the densities derived for the Burrows et al. model is problematic. The settling time for such particles, for the gas density at 100 au in the Betal model ( $4 \times 10^{-17} \text{ g cm}^{-3}$ ), is only about  $10^4$  yr (e.g., Weidenschilling 1977, Epstein regime). It may be that the observed dust is dynamically maintained, e.g., by interaction of a wind with the disk, or is merely the remnant of a much greater amount of dust that has already coagulated and settled to the midplane. Note also that if the density profile extended smoothly to larger radii, there would be significantly more obscuration along the line of sight to the central axis of the source. Therefore, if the density profile inferred by Betal is correct, the disk must be truncated or make a transition to a significantly steeper density law at 250 au. An abrupt truncation is also inferred from the observed radial intensity profiles in the Orion disks as analyzed by McCaughrean & O'Dell (1996), which are discussed below.

McCaughrean & O'Dell (1996, hereafter MCODE) present *HST* images of six backlit disk silhouettes in the Orion

Nebula that range in radius from 25 to 500 au. By modeling major axis intensity profiles of the five not viewed edge-on, MCODE argue that these disks are abruptly truncated with a steeper surface density power law,  $\Sigma \propto r^{-4}$ , than is likely to exist throughout most of the disk. The largest disk, 114 – 426, is viewed nearly edge-on. We display in Figure 10 silhouette models for this disk that result from using two different density profiles; this figure is to be compared to the emission line composite images in MCODE (continuum images are dominated by scattered light from the central star not modeled in this figure). This figure was constructed by integrating  $\kappa \rho dz$  along lines of sight through an assumed axisymmetric density distribution with the HS optical opacity of  $71.6 \text{ cm}^2 \text{ g}^{-1}$ . Lines are contours of equal intensity where  $I/I_0 = e^{-\tau} = 0.75, 0.5, 0.25$ , and  $0.1$ ; the  $0.5$  contour where  $\tau = \frac{2}{3}$  is highlighted. The solid line contours result from a model based on the MCODE truncation surface density law. The model has a midplane density profile of  $\rho_m = 6 \times 10^{-15} \text{ g cm}^{-3} (r/100 \text{ au})^{-5.5}$ , which, with an isothermal scale height, corresponds to  $\Sigma \propto r^{-4}$ . The model is truncated at 500 au. The vertical distribution of density results from a hydrostatic, isothermal atmosphere at 50 K for a stellar mass of  $M_* = 1 M_{\odot}$  (or equivalently 25 K with  $M_* = \frac{1}{2} M_{\odot}$ ). The radial density profile of the model corresponding to the dashed lines is based on the Betal model for HH30 in which  $\rho_m = 4.1 \times 10^{-17} \text{ g cm}^{-3} (r/100 \text{ au})^{-2.2}$ . The model has been extended out to 500 au and abruptly truncated.

For such systems, the line-of-sight optical depth throughout the silhouette is dominated by the distribution of material in the outermost part of the disk. Both models give

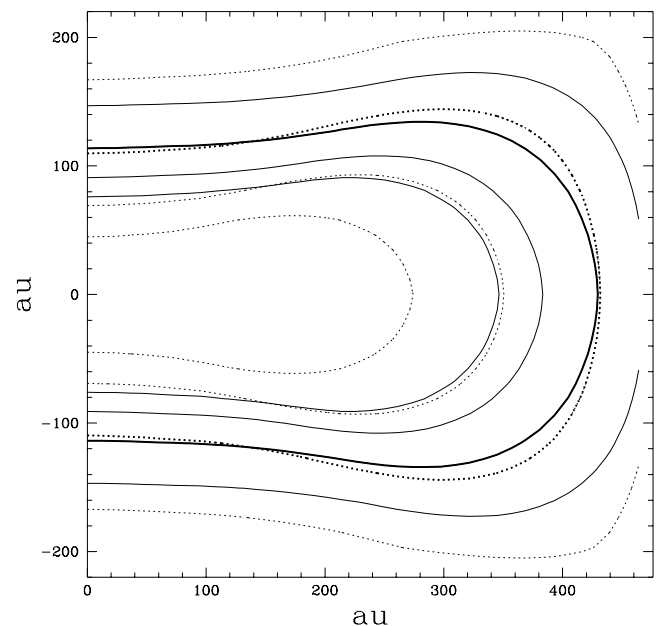


FIG. 10.—Edge-on disk silhouettes. Contours are based on integrated line-of-sight optical depths in axisymmetric density distributions where  $I/I_0 = e^{-\tau} = 0.75, 0.5$  (highlighted:  $\tau_{0.66} = \frac{2}{3}$ ),  $0.25$  and  $0.1$ . The dashed contours are based on the vertical and radial density structure derived by Burrows et al. (1997) for HH30, which has been extended to 500 au. The solid contours represent a model with a radial density profile of  $\rho \propto r^{-5.5}$ , compatible with the truncation law  $\Sigma \propto r^{-4}$  derived by McCaughrean & O'Dell (1996) for five Orion face-on systems. The vertical density profile is that of an isothermal atmosphere at 50 K hydrostatically supported against a stellar potential of  $1 M_{\odot}$ .

approximately the correct half thickness of 110 au. (Notice that the silhouette shows an apparent thickness considerably greater than its scale height; the pressure scale height for the hydrostatic model is only about 65 au at a radius of 350 au, where the apparent thickness is more than 110 au.) Both models have nearly the same midplane density at 500 au ( $\approx 10^{-18}$  g cm $^{-3}$ ). The steeper midplane density profile produces a flatter image qualitatively more like the observed shape of the 114–426 silhouette; the flatter image occurs because high densities lie at only slightly smaller radii and contribute significantly to the line-of-sight optical depth along the axis of the system. The model based on HH30 also shows considerably softer intensity gradients in both radial and vertical directions than the steeper density profile models. This softer profile is required to reproduce the scattered light from the star seen along the axis of the system. The effect of the *HST* point spread function will only further soften the idealized profiles shown in Figure 10. The major axis cut of 114–426 (cf. their Fig. 4) shows significant asymmetry: On one side, the steepest part of the intensity profile covers about 90 au, while on the other side the profile is both considerably shallower and covers a much larger radial range ( $> 350$  au). While neither model in Figure 10 is ruled out because of this asymmetry, the steeper density profile model has a radial intensity range from  $I/I_0 = 0.1$  to 0.75 of 100 au consistent with the range of the steeper side of the 114–426 profile. This qualitative modeling suggests that the 114–426 disk may have the same radial density profile seen in the five face-on Orion disks with a thickness compatible with uniform illumination.

## 6. CONCLUSIONS

In this work we have calculated vertical structure models of circumstellar accretion disks in an attempt to address problems of disk shape, illumination, and appearance. We distinguish between the inner viscously active disk and the outer disk, which is optically thin to its own radiation. In the viscously active part of the disk, we find that the Rosseland mean photosphere generally increases in relative thickness,  $H_R/r$ , out to a radius defined by the condensation of dust grains. Inside this shadow radius, reprocessing of central object photons will be greater than expected from the pure flat disk analysis. Beyond the shadow radius, the photosphere turns concave downward, shielding most of the disk from illumination by either star or FU Orionis outburst. All but the longest wavelengths tested peak in  $H_\lambda/r$  at the same radius at which the Rosseland mean  $H_R/r$  peaks. Note that line-of-sight extinction for rays traveling nearly parallel to the disk's surface through the  $\tau < \frac{2}{3}$  atmosphere above the disk's surface will limit stellar reprocessing to a radius even smaller than the idealized "shadow radius." Calculations in this work assume that mass flux through the disk is constant at all radii. In the outer parts of realistic disks where mass flows outward carrying away angular momentum released by the inner disk, our conclusion of shadowing will only be reinforced because the radially dropping viscous energy generation there results in a colder, thinner disk beyond the turn-around radius.

Radial trends in the shape of the viscous disk (as well as midplane temperature, surface density, and optical depth) are controlled by the temperature exponent of the opacity. At the lowest mass flux tested:  $\dot{M} = 10^{-9} M_\odot \text{ yr}^{-1}$ , the peak in  $H_R/r$  is smaller than a stellar radius. These highly depleted systems will reprocess energy at essentially the flat

disk rate out to the radius at which the disk becomes optically thin to its own radiation. Coagulation of opacity producing particles throughout the history of the nebula will also increase disk flaring. These findings suggest a non-monotonic thermal history for primordial bodies in the disk at several au. At early times, when disk mass fluxes are large, annuli at this radius will be shadowed from central object radiation and heated principally by local energy dissipation. At late times when nebular mass flux has decreased due to depletion of the surrounding envelope and outer disk and significant particle coagulation has modified the local opacity law, bodies at a few au will become exposed to radiation from the central star. Back scattering from a cocooning envelope has not been taken into account in this calculation. The reradiation of photons captured high up in the envelope back onto the disk may cause significant heating of the disk even beyond its peak in relative thickness. This process is likely to be especially important during the early stages of nebular evolution when the envelope extends in to small radius (Chick & Cassen 1997; d'Alessio et al. 1997). Future work will address this contribution in a self-consistent manner.

All of the observations made so far of protostellar systems are sensitive only to large radii where disks are vertically optically thin to their own radiation. It is not clear whether this part of the disk will be subject to the same form of turbulent energy generation probable in the inner optically thick disk. Because both accretion temperature and stellar reprocessing fall off as  $r^{-3/4}$ , even the highest mass flux disks will be dominated by a background radiation source of 10 or 20 K well within a hundred au. The energetics of these outer disks are therefore likely to be dominated by the ambient radiation field and consequently vertically and radially isothermal. Pressure scale heights in isothermal disks flare strongly:  $h \propto r^{3/2}$ . While these outer disks are vertically optically thin to their own radiation as well as to all but the shortest wavelength radiation, when seen edge-on, they can appear quite optically thick. Both HH30 as modeled by Betal and the Orion silhouettes observed by MCOD are consistent with isothermal disks hydrostatically supported against the potential of the central object. Interestingly, the two studies may suggest different radial density profiles; both clearly suggest abrupt truncation. When no longer constrained by the constant mass flux assumption, there is no obvious theoretical argument for what the density distribution of a disk should be. Commonly assumed profiles (e.g.,  $\Sigma \propto r^{-3/2}$  Beckwith et al. 1990) that have been used to estimate disk mass and optical depth are apparently not supported by current observational estimates.

The authors would like to acknowledge helpful suggestions from Steve Ruden and the mentorship of Peter Bodenheimer. Thanks are given to Ralph Stognienko for the wavelength-dependent opacities in computerized form. K. R. B. thanks the Max Planck Society for financial support during her two stays at the Max Planck Research Unit in Jena. This work was supported in part by Origins grant NAGW 4456 and was conducted under the auspices of a special NASA Astrophysics Theory Program that supports a Joint Center for Star Formation Studies at NASA Ames Research Center, the University of California at Berkeley, and the University of California at Santa Cruz.

## APPENDIX A

A GENERAL CONSTRAINT ON  $\beta$  FOR CONVECTION

A constraint on  $\beta$  similar to what was found by Lin & Papaloizou for a specific homologously contracting disk solution is found in the following general derivation, which assumes only that the local energy generation is either positive or zero (i.e., there are no energy sinks). Begin with radiative (diffusive) flux transport:

$$F = \frac{4acT^3}{3\kappa\rho} \frac{\partial T}{\partial z}. \quad (\text{A1})$$

The vertical change in flux  $\partial F/\partial z$  is set by the local energy generation  $q^+$ . Let  $\kappa = \kappa_n T^\beta$ , and take the ideal gas law  $\rho = \mu P/R_g T$ . Differentiation of equation (A1) with respect to  $z$  results in terms with  $(\partial T/\partial z)$ ,  $(\partial P/\partial z)$ ,  $(\partial \mu/\partial z)$ , and  $(\partial^2 T/\partial z^2)$ . We have hydrostatic support and the definition of  $\nabla$ :

$$\frac{\partial P}{\partial z} = -\rho\Omega^2 z, \quad (\text{A2})$$

$$\nabla \equiv \frac{\partial \log T}{\partial \log P}. \quad (\text{A3})$$

Assuming rotation constant on cylinders the first and second vertical derivatives of the temperature are

$$\frac{\partial T}{\partial z} = -\Omega^2 z \nabla \frac{\mu}{R_g}, \quad (\text{A4})$$

$$\frac{\partial^2 T}{\partial z^2} = -\frac{\Omega^2}{R_g} \left( \mu \nabla + z \nabla \frac{\partial \mu}{\partial z} + \mu z \frac{\partial \nabla}{\partial z} \right). \quad (\text{A5})$$

The  $\partial \mu/\partial z$  terms exactly cancel (their effect is retained in the  $\partial \nabla/\partial z$  term). By requiring  $q^+ \geq 0$ , we find

$$0 \leq (4 - \beta) \nabla - 1 - \left( \frac{c_s}{\Omega z} \right)^2 \left( 1 + \frac{\partial \log \nabla}{\partial \log z} \right), \quad (\text{A6})$$

or equivalently

$$\nabla \geq \frac{1}{4 - \beta} \left[ 1 + \left( \frac{c_s}{\Omega z} \right)^2 \left( 1 + \frac{\partial \log \nabla}{\partial \log z} \right) \right] \equiv \nabla_\beta. \quad (\text{A7})$$

For convection  $\nabla > \nabla_{ad}$ . Convection therefore exists in any annulus for which  $\nabla_\beta > \nabla_{ad}$ :

$$\beta > 4 - \frac{1}{\nabla_{ad}} \left[ 1 + \left( \frac{c_s}{\Omega z} \right)^2 \left( 1 + \frac{\partial \log \nabla}{\partial \log z} \right) \right]. \quad (\text{A8})$$

Convection is not favored at the midplane, where buoyancy due to the vertical component of gravity disappears. Cases in which convection crosses the midplane (e.g., Kley et al. 1993) are due to overshoot of convective motions initiated some distance above. Well above a pressure scale height where  $z \gg c_s/\Omega$ , equation (A8) reduces to exactly the formula derived by Lin & Papaloizou (1980). The second term may, however, provide significant modification for the constraint on  $\beta$  from the Lin & Papaloizou value. In particular, the  $\partial \log \nabla/\partial \log z$  term will depend on the distribution of local heat sources. In the case of a polytrope where  $P \propto T^\gamma$ , this term is clearly zero. The meaning of the term in the viscous disk case, however, is not clear. If this term can be assumed to be small (the generally small  $\nabla$  gradient found in numerical results such as those shown in Figure 8 is supportive of this assumption), one finds that at one pressure scale height above the midplane where  $z \approx c_s/\Omega$ , equation (A8) reduces to

$$\beta > 4 - \frac{2}{\nabla_{ad}} = \frac{2\gamma - 4}{\gamma - 1} = -3 \quad (\text{A9})$$

for  $\gamma = 7/5$ . This is a less restrictive value than the Lin & Papaloizou result of  $\frac{1}{2}$  and suggests that convection may be even more prevalent than suggested by the earlier derivation. Although strongest at annuli where a given particle species exists all the way down to the midplane, results presented in Figure 7 indeed show the existence of convective motions at some level at all radii beyond the dust condensation front (marked by narrow diamonds).

## REFERENCES

- |  |  |
|--|--|
| <p>Adams, F. C., Lada, C. J., &amp; Shu, F. H. 1987, <i>ApJ</i>, 312, 788<br/>         Adams, F. C., Ruden, S. P., &amp; Shu, F. H. 1989, <i>ApJ</i>, 347, 959<br/>         Adams, F. C., &amp; Shu, F. H. 1985, <i>ApJ</i>, 296, 655<br/>         Beckwith, S. V. W., Sargent, A. I., Chini, R. S., &amp; Güsten, R. 1990, <i>AJ</i>, 99, 924<br/>         Bell, K. R., &amp; Lin, D. N. C. 1994, <i>ApJ</i>, 427, 987 (BL)</p> | <p>Bodenheimer, P. H., Yorke, H. W., Różyczka, M., &amp; Tohline, J. E. 1990, <i>ApJ</i>, 355, 651<br/>         Boss, A. 1993, <i>ApJ</i>, 417, 351<br/>         Burrows, C. J., et al. 1996, <i>ApJ</i>, 473, 437 (Betel)<br/>         Cabot, W. 1996, <i>ApJ</i>, 465, 874<br/>         Cassen, P. M. 1993, <i>Lunar &amp; Planet. Sci. Conf.</i>, XXIV, 261</p> |
|--|--|

- Cassen, P. M. 1994, *Icarus*, 112, 405  
 Cassen, P. M., & Moosman, A. 1981, *Icarus*, 48, 353  
 Chandrasekhar, S. 1961, *Hydrodynamic and Hydromagnetic Stability* (Oxford: Clarendon Press)  
 Chick, K. M., & Cassen, P. M. 1997, *ApJ*, 477, 398  
 Chick, K. M., Pollack, J. B., & Cassen, P. M. 1996, *ApJ*, 461, 956  
 Close, L. M., Roddier, F., Northcott, M. J., Roddier, C., & Graves, J. E. 1997, *ApJ*, 478, 766  
 d'Alessio, P., Calvet, N., & Hartmann, L. W. 1997, *ApJ*, 474, 397  
 Hartmann, L., & Kenyon, S. J. 1996, *ARA&A*, 34, 207  
 Henning, Th., & Stognienko, R. 1996, *A&A*, 311, 291 (HS)  
 ———, 1997, Opacity tables included in <http://www.astro.uni-jena.de/Users/stog/Opacities/opacities.html>  
 Kawazoe, E., & Mineshige, S. 1994, *PASJ*, 45, 715  
 Kenyon, S. J., & Hartmann, L. W. 1987, *ApJ*, 323, 714  
 Kley, W., Papaloizou, J. C. B., & Lin, D. N. C. 1993, *ApJ*, 416, 679  
 Lay, O. P., Carlstrom, J. E., Hills, R. E., & Phillips, T. G. 1994, *ApJ*, 434, L75  
 Levermore, C. D., & Pomraning, G. C. 1981, *ApJ*, 262, 768  
 Lin, D. N. C., & Papaloizou, J. 1980, *MNRAS*, 191, 37  
 ———, 1985, in *Protostars and Planets II*, ed. D. C. Black & M. S. Matthews (Tucson: Univ. Arizona Press), 981  
 Lüst, R. 1952, *Z. Nat.*, 7a, 87  
 Lynden-Bell, D., & Pringle, J. E. 1974, *MNRAS*, 168, 603  
 Malbet, F., & Bertout, C. 1991, *ApJ*, 383, 814  
 McCaughrean, M. J., & O'Dell, C. R. 1996, *AJ*, 111, 1977 (MCOB)  
 Men'shchikov, A. B., & Henning, Th. 1997, *A&A*, 318, 879  
 Men'shchikov, A. B., Henning, Th., & Fischer, O. 1997, in preparation  
 Meyer, F., & Meyer-Hofmeister, E. 1982, *A&A*, 106, 34  
 Mihalas, D. 1978, *Stellar Atmospheres* (San Francisco: Freeman)  
 Morfill, G. E., & Wood, J. A. 1989, *Icarus*, 82, 225  
 Mucha, R. 1996, private communication  
 Mundy, L. G., Wootten, H. A., & Wilking, B. A. 1990, *ApJ*, 352, 159  
 Mundy, L. G., et al. 1996, *ApJ*, 464, L169  
 Pollack, J. B., Hollenbach, D., Beckwith, S., Simonelli, D. P., Rousch, T., & Fong, W. 1994, *ApJ*, 421, 615  
 Pringle, J. E. 1981, *ARA&A*, 19, 137  
 Różyczka, M. N., Bodenheimer, P. H., & Bell, K. R. 1994, *ApJ*, 423, 736  
 Ruden, S. P., & Lin, D. N. C. 1986, *ApJ*, 308, 883  
 Ruden, S. P., & Pollack, J. B. 1991, *ApJ*, 375, 740  
 Ryu, D., & Goodman, J. 1992, *ApJ*, 338, 438  
 Safronov, V. S. 1960, *Ann. d'Astrophys.*, 23, 979  
 Schmitt, W., Henning, Th., & Mucha, R. 1997, *A&A*, in press  
 Shakura, N. I., & Sunyaev, R. A. 1973, *A&A*, 24, 337  
 Stapelfeldt, K. R., et al. 1995, *ApJ*, 449, 888  
 Stemwedel, S. W., Yuan, C., & Cassen, P. 1990, *ApJ*, 351, 206  
 Stone, J. M., & Balbus, S. A. 1996, *ApJ*, 464, 364  
 Strom, S. E., Edwards, S., & Skrutskie, M. F. 1993, in *Protostars and Planets III*, ed. E. H. Levy & J. Lunine (Tucson: Univ. Arizona Press), 837  
 Tomley, L., Cassen, P. M., & Steinman-Cameron, T. 1991, *ApJ*, 382, 530  
 Toomre, A. 1964, *ApJ*, 139, 1217  
 Turner, N. J. J., Bodenheimer, P., & Bell, K. R. 1997, *ApJ*, 480, 754  
 van Dishoeck, E. F., Blake, G. A., Draine, B. T., & Lunine, J. I. 1993, in *Protostars and Planets III*, ed. E. H. Levy & J. Lunine (Tucson: Univ. Arizona Press), 163  
 Weidenschilling, S. J. 1977, *MNRAS*, 180, 57